An Interfacial and Bulk Charge Transport Model for Dye-Sensitized Solar Cells Based on Photoanodes Consisting of Core–Shell Nanowire Arrays

Justin J. Hill,[†,‡] Nick Banks,[†] Kelly Haller,[†] Mark E. Orazem,[†] and Kirk J. Ziegler*,[†,¶]

[†]Department of Chemical Engineering, University of Florida, Gainesville, Florida 32611, United States
[¶]Center for Surface Science and Engineering, University of Florida, Gainesville, Florida 32611, United States

S *Supporting Information*

ABSTRACT: Dye-sensitized solar cells (DSSCs) based on ordered photoanode morphologies, such as nanotubes and nanowires, are widely gaining attention because these geometries are believed to enhance interfacial charge transfer and bulk charge transport. Unfortunately, experimental results have yet to show substantial improvement to conversion efficiency over nanoparticle-based DSSCs. A model is developed to characterize the performance of an idealized photoanode based on an ordered array of transparent conductive nanowires coated with an anatase titania shell. The role of the interfacial electric field in nanowire-based DSSCs is explored computationally by turning electron migration ON or OFF. The results show that back-reaction rates are most strongly influenced by the electric field. These electron loss mechanisms can be reduced by several orders of magnitude, leading to improvements in short-circuit current, open-circuit voltage, and fill factor.
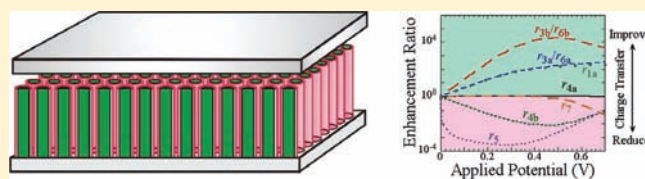
INTRODUCTION

Dye-sensitized solar cells (DSSC) are traditionally based on films of titania nanoparticles (NP-DSSC).[1] These devices mimic photosynthesis and currently have achieved conversion efficiencies in excess of 11%.[2] They can be fabricated at lower costs than silicon-based photovoltaics, making them an attractive alternative for producing low-cost, clean energy.[3–5] Additionally, DSSCs have been shown to outperform silicon-based photovoltaics on cloudy days.[6]

The interfacial kinetics and energy levels of the heterogeneous components of traditional NP-DSSCs are designed to optimize performance.[1,4,7] The maximum output voltage is determined by the difference between the flat-band potential of the semiconductor and the electrochemical potential of the electrolyte, E_{REDOX}. Once an electron is photoexcited from the highest occupied molecular orbital of the dye (HOMO) to the lowest unoccupied molecular orbital (LUMO), the electron can either relax back to the ground state, be injected into the semiconductor layer, or back-react with the electrolyte. Most electrons should be injected into the semiconductor region to achieve maximum performance; however, loss of photogenerated electrons to the electrolyte is energetically favorable. Therefore, the kinetics of electron injection into the semiconductor must be much faster than electron loss to the electrolyte (10^{13} vs 10^2 s^{-1}). The electrolyte can be modified to increase the REDOX potential, but this typically increases the rate of back reaction.[8] Therefore, the requirement that reactions be controlled by kinetics rather than thermodynamics results in lower output potential of the cell.

When the interface of a DSSC is illuminated, an excess of positive charge will build up in the space-charge layer of the n-type semiconductor. This accumulation in the space-charge layer helps establish an interfacial electric field that separates charge. However, Figure 1a shows that this field will disappear at a finite, and nonzero, nanoparticle diameter. This field becomes negligible for particle sizes below ~30 nm[9] such that typical DSSC systems have the flat-band potential illustrated in Figure 1b. In addition, Figure 1a shows that any charge driven into the center of the particle by this field experiences a barrier to transport out of the nanoparticle. Therefore, electron transport in the porous, nanocrystalline photoanode of the NP-DSSC is governed by trap-limited diffusive transport of conduction band electrons on the surface of the nanoparticle.[10–15] Unfortunately, the competing relationship between electron diffusion and lifetime limits the electron diffusion length to about 10 μm within a nanoparticle film.[11] Attempts to increase photocurrent by fabricating nanoparticle photoanodes with dimensions in excess of 10 μm are often futile because almost none of the electrons generated in this region are collected.[11,16–18]

The limits of NP-DSSCs have led researchers to investigate nanowire-based DSSCs (NW-DSSCs) as an alternative configuration for the photoanode. In these systems, an interfacial electric field is established that is not present in NP-DSSCs. This field aids interfacial charge transfer and minimizes electron loss.[19–22] However, the effect of the electric field diminishes as
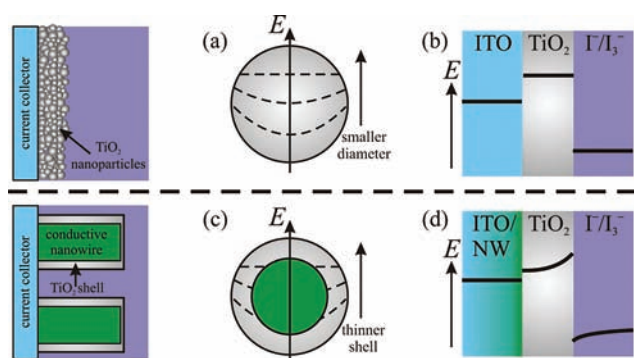
**Figure 1.** Schematic comparison of the energy level diagrams for the semiconductor−dye−electrolyte interface of DSSCs based on (top) titania nanoparticles and (bottom) titania core−shell nanowires. The energy levels within the nanoparticle and shell are shown in (a) and (c), respectively. The resulting energy level diagrams for the devices are shown in (b) and (d), respectively.

the diameter of the nanowire decreases, leading several researchers to investigate conductive core−semiconductive shell nanowires in order to enhance axial transport of electrons.[21−24] Figure 1c shows that these core−shell nanowire systems exhibit the same charge buildup at the semiconductor−electrolyte interface. However, the direct electrical contact of the core to the current collector allows the charge to be removed from the titania layer without going through the potential energy barrier that NP-DSSCs experience. Therefore, an electric field is established that helps separate the charge at the interface and drive the electrons to the nanowire core, as shown in Figure 1d. Even in the absence of this field, the probability of radial electron transport to the conductive core followed by axial transport is higher than axial transport of electrons solely through the titania shell or on its surface to the current collector. This preferential direction in transport is especially important for electrons injected at lengths greater than an electron can diffuse to the current collector.[11,16−18] Therefore, electrons are expected to preferentially flow radially toward the nanowire core. Due to the rapid transport of electrons in the conductive core, it is believed that injected electrons in even small core−shell nanowires will be driven to the core. This effectively decouples charge collection distance from photoanode thickness and allows for photoactive surface area (and photogenerated current) to be increased beyond the current transport-driven limitations of NP-DSSCs.

Mathematical models of NP-DSSCs that account for interfacial reaction dynamics and energy levels have been developed in conjunction with dynamic response measurements.[8,16,25,26] Both discrete and continuum-based computations indicate that the transport of electrons within the nanoparticle photoanode is purely diffusive.[11,13−15] Furthermore, the overall performance of NP-DSSCs has been accurately predicted through both a continuum model of the photoanode[15] and a circuit model of the photoelectrochemical cell.[12] Although the performance and dynamics of NP-DSSCs can be calculated, no comparable models exist for the NW-DSSC. To our knowledge, this paper describes the first model that can predict the overall behavior of DSSCs based on nanowire photoanodes composed of a conductive core and a semiconductive shell. The model is used to illustrate how the interfacial processes are affected by the electric field and conductive core present in core−shell NW-DSSCs and, thus, only includes the dominant routes of charge transport in the
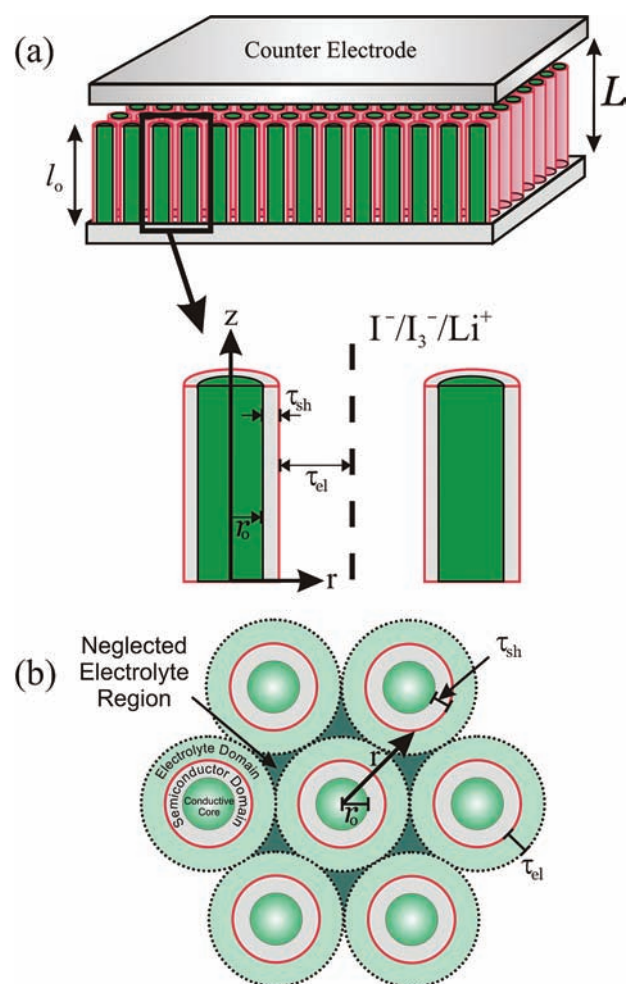
Figure 2. (a) Side-view and (b) top-view schematic diagrams of the nanowire photoanode. The nanowires are coated with a semiconductor shell and surrounded by an electrolyte. Only a cylindrical shell of electrolyte is considered.

radial direction. The electric field in the system is not artificially imposed, but arises solely as a result of charge carrier distributions in the semiconductor through diffusion and migration. As such, the thickness of the shell significantly alters the electric field gradients. The effect of the field and conductive core is quantified by eliminating migrational contributions to electron transport and comparing the changes to interfacial reactions and overall performance. The results show that back-reaction rates can change by as much as 4 orders of magnitude in the presence of an electric field.

■ MODEL DEVELOPMENT

The structure of the photoanode, shown in Figure 2a, consists of transparent conductive nanowires with high aspect ratios. The nanowires are coated with a conformal semiconductive layer and a photoactive dye. The nanowire array is immersed in a REDOX electrolyte, which for the purposes of these computations only includes a cylindrical shell of electrolyte. Therefore, there is a small region between the nanowires that is neglected, as is shown in Figure 2b. The coaxial nanowire has a conductive core of radius r_o and length l_o, a semiconducting shell (sh) that is bounded between $r \in [r_o, r_o + \tau_{sh}]$ and $z \in [0, l_o]$ and a

surrounding electrolyte region (el) bounded between $r \in [r_o + \tau_{sh}, r_o + \tau_{sh} + \tau_{el}]$ and $z \in [0, l_o]$, where τ_{sh} is the semiconductor shell thickness and τ_{el} is half of the nanowire—nanowire spacing. The distance separating the current collector from the counter electrode is given by L. Because the array consists of closely packed nanowires with high aspect ratios, any contributions to photovoltaic performance from the tips of the nanowires or the semiconductor—TCO substrate (i.e., the bottom of the photoanode) were neglected since the planar surface area contributes only a minor fraction of the total photoactive surface area. The electrolyte was taken to be an iodide/triiodide system (I^-/I_3^-), with Li^+ as the counterion.

Key components of the NW-DSSC, such as carrier concentration, potential, flux of charge carriers, and electrolyte concentration, are dependent on the radial and axial dimensions. However, scaling arguments simplify the mathematics and decrease computational expense. The spatial coordinates were scaled such that $\tilde{Z} = z/l_o$, $\tilde{R}_{el} = (r - r_o - \tau_{sh})/\tau_{el}$, and $\tilde{R}_{sh} = (r - r_o)/\tau_{sh}$, where $\tilde{Z}$ is the dimensionless length scale in the z-direction and $\tilde{R}_{el}$ and $\tilde{R}_{sh}$ are the dimensionless length scales in the radial direction for the electrolyte and semiconductor, respectively. In this study, the lengths of the nanowires (l_o) were on the order of $1-10\,\mu$m and the semiconducting (τ_{sh}) and electrolyte (τ_{el}) regions were on the order of 10 nm. Therefore, for any function, $\mathscr{F}(\tilde{R}_j, \tilde{Z})$, the differential operator $\vec{\nabla} = \hat{\mathbf{r}}(\partial/\partial r) + \hat{\mathbf{z}}(\partial/\partial z)$ can be approximated by

$$\vec{\nabla}\mathscr{F} = \frac{1}{\tau_j}\left(\hat{\mathbf{r}}\frac{\partial}{\partial \tilde{R}_j} + \frac{1}{a_j}\hat{\mathbf{z}}\frac{\partial}{\partial \tilde{Z}}\right)\mathscr{F} \simeq \frac{1}{\tau_j}\hat{\mathbf{r}}\frac{\partial}{\partial \tilde{R}_j}\mathscr{F} \qquad (1)$$

and similarly ∇^2 becomes

$$\nabla^2\mathscr{F} = \frac{1}{\tau_j^2}\left(\frac{\partial}{\partial \tilde{R}_j^2} + \frac{1}{a_j^2}\frac{\partial}{\partial \tilde{Z}^2}\right)\mathscr{F} \simeq \frac{1}{\tau_j^2}\frac{\partial^2}{\partial \tilde{R}_j^2}\mathscr{F} \qquad (2)$$

where $a_j = l_o/\tau_j$ is the aspect ratio associated with the semiconductor and electrolyte regions.

Equations 1 and 2 provide reasonable approximations if the gradient of the state variables in the axial direction are on the same order or smaller than changes to those variables in the radial direction. The distance over which large changes to the state variables (i.e., potential, concentration, etc.) occur is determined by the region where charge density varies dramatically, which is correlated to the Debye length. For an electrolyte, the Debye length, $\lambda_{D,el}$, is given by

$$\lambda_{D,el} = \left[\frac{\varepsilon_{el}RT}{F^2 \sum\limits_i z_i^2 C_{i,\infty}}\right]^{1/2} \qquad (3)$$

where $C_{i,\infty}$, ε_{el}, and z_i are the bulk (reference) concentrations of the electrolyte ions, the electrolyte permittivity and the charge of the electrolyte species, respectively. Typically, the value of the charge density approaches zero at a distance of roughly $10-20\lambda_{D,el}$ from the interface. Using reasonable values for the electrolyte, eq 3 yields $\lambda_{D,el} = 0.95$ nm. Thus, the diffuse region of charge will have a thickness of approximately 20 nm.

Similarly, the Debye length for the semiconductor, $\lambda_{D,sh}$, can be written as

$$\lambda_{D,sh} = \left[\frac{\varepsilon_{sh}RT}{F^2(\hat{N}_d + \hat{N}_a)}\right]^{1/2} \qquad (4)$$

where $\hat{N}_d$ and $\hat{N}_a$ are the donor and acceptor concentrations, respectively, and F is Faraday's constant. Equation 4 yields $\lambda_{D,sh} = 28.2$ nm. The width of the space-charge region in the semiconductor is a factor of $(2FV/RT)^{1/2}$ larger than the Debye length. This factor is equal to 6.84 for an interfacial potential drop of 0.6 V (the dark interfacial potential difference of a NP-DSSC),[10] yielding a space-charge region thickness of approximately 200 nm in the semiconductive shell of the nanowire. These values are consistent with the expectation that the depletion region is much larger in a semiconductor than an electrolyte when the two are in electrical contact.

The Debye lengths calculated from eq 3 and 4 suggest that the approximations given by eq 1 and 2 may not be valid in the semiconductor within 200 nm of the ITO current collector or within 20 nm of the ITO in the electrolyte. However, these regions only encompass 1% of the total photoactive surface area for nanowires with lengths of 10 μm and diameters of 200 nm.

An anodic half-cell DSSC encompasses three domains: (i) the semiconductor—dye—electrolyte interface, (ii) the semiconductor, and (iii) the electrolyte. Therefore, the model includes the equations that govern the physics of these three distinct regions. An interfacial kinetic model presented below shows the interaction of charge carriers with the dye, electrolyte, and semiconductor interfacial states. The bulk charge carrier transport through the semiconductor shell and electrolyte are then modeled as having a position-dependent distribution of charge carrier density, which can give rise to an electric field that sweeps charge carriers preferentially to the current collector (conductive nanowire core). To evaluate the current—voltage profile, the interfacial model is coupled with the equations of bulk charge transport and potential distribution within both the semiconductor and electrolyte. A list of variables and constants used for this study are presented in Tables S1—S5 (Supporting Information [SI]).

INTERFACIAL KINETICS

The generation and transfer of charge at the semiconductor—dye—electrolyte interface involves a complex arrangement of series and parallel reaction pathways. As shown in Figure 3a, it is assumed that the titania covers completely the conductive core of the nanowire. However, the photoactive dye may not cover the entire surface of the titania layer. Therefore, charge transport can occur between the electrolyte and either the dye or titania. Charge transfer reactions mediated through photoexcitation of charge within the dye either: (1) produce the desired anodic reaction (electron injection into the semiconductor) or (2) serve as a localized cathode, resulting in no usable conversion of solar energy (i.e., back react). The various states that exist in each region of the DSSC and the reactions between them are illustrated in Figure 3b. The dye exists at the interface and has both a singlet (S_1^*) and triplet excited state (S_3^*). Electrons in the semiconductor region may have energies associated with the valence (VB) and conduction bands (CB) as well as trap states (t). The inner surface state (ISS) represents a plane of charge associated with electrons occupying surface states, and the outer surface state (OSS) represents a plane of closest approach for electrons in the space-charge region. An analogous description is applied for the electrolyte, where the inner Helmholtz plane (IHP) is associated with adsorbed ions and the outer Helmholtz plane (OHP) is the plane of closest approach for hydrated ions in the diffuse region of charge.
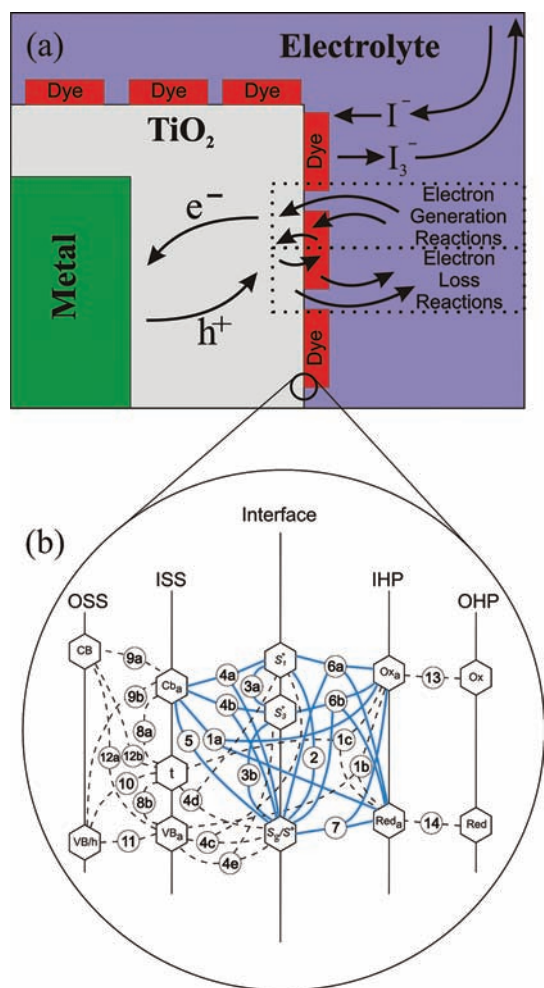
Figure 3. (a) Schematic diagram for modeling the charge transport in NW-based DSSCs with an electric field. The electron is injected into the titania layer while the hole is injected into the electrolyte. (b) At the interface of the electrolyte and nanostructures, numerous reactions can occur between the dye, electrolyte, and semiconductor regions. The paths shown in blue are the kinetic reactions modeled in this study. States are defined as: OHP/IHP = Outer/Inner Helmholtz Plane; OSS/ISS = Outer/Inner Surface States; Ox/Red = Oxidized/Reduced Electrolyte Atom; S_1^*/S_3^* = excited dye states; S_g/S^+ = dye in ground/reduced state; VB/CB = valence/conduction band state; a = adsorbed species.

Multiple charge-transfer reactions can occur between these energy states as shown by the lines connecting each state in Figure 3b. However, only reactions 1–7 (marked in blue in Figure 3b) are considered in the present work because these reactions produced a good correlation with experimental data for NP-DSSCs.[14,15] The specific reactions occurring between these states are presented in Table 1. The reactions listed in Figure 3b follow those developed by Penny et al.,[14] with the exception that the effect of surface area is taken into account. They are outlined here for clarity using general notation.[27] Reactions r_2, r_{3a}, and r_{3b} do not depend on potential as they occur within a given plane of charge; otherwise, the rate of a generic reaction can be written as

$$r_l = k_{\mathrm{f},l} e^{b_a \Delta \phi_l} \prod_i C_i^{p_{i,l}} - k_{\mathrm{b},l} e^{-b_c \Delta \phi_l} \prod_i C_i^{q_{i,l}} \qquad (5)$$

The generic rate of reaction, r_l, has forward and backward reaction rate constants, $k_{\mathrm{f},l}$ and $k_{\mathrm{b},l}$, as well as the anodic and cathodic exponential constants, $b_a = (1 - \alpha)nF/RT$ and $b_c = \alpha nF/RT$. The reaction energetics are assumed to be symmetric about the activation energy (i.e., $\alpha = 1/2$ so that $b_a = b_c = 19.47n$ V^{-1}). The reaction orders, $p_{i,l}$ and $q_{i,l}$, are related to the stoichiometric coefficients, $s_{i,l}$, which are defined by[27]

$$s_{i,l} = \begin{cases} p_{i,l} & \text{for } s_{i,l} > 0 \\ -q_{i,l} & \text{for } s_{i,l} < 0 \end{cases}$$

This interfacial model neglects the surface charge due to adsorbed charge carriers and ions that would be described in a model of the double layer at the electrolyte and semiconductor interface, respectively. The only adsorbed charge species included is the oxidized state of the dye. In addition, this study did not consider surface trap states or the conduction of holes. The concentration of vacancies in the conduction band was balanced by the density of conduction band states and the concentration of electrons, $C_\gamma = \Gamma - C_e$. This constraint ensures that the number of electrons does not exceed the number of available states. In writing this equation, it is assumed that photoexcitation within the semiconductor is negligible when compared to electron injection by the sensitizer.

The following discussion highlights the fundamental components to aid comprehension of the model as a whole as well as highlight the primary departures from the interfacial model previously reported by Penny et al.[14] The primary difference between the rates listed in Table 1 from prior work is that these rates are dependent on the nanowire length, l_o, rather than the surface area to volume ratio, S_V. Therefore, the total rates of reaction increase with longer nanowires. Higher densities of nanowires also correspond to an increase in the total rates of reaction. The total current density, i, was then obtained by integrating over the nanowire length.

Reaction 1a (Table 1) represents the dark current (electrolyte-semiconductor charge transfer) that passes across the fraction of exposed semiconductor surface given by $1 - \theta$, where θ is the fractional semiconductor surface coverage of the photoactive dye. Reaction 2 (Table 1) accounts for the photoexcitation of a ground state dye molecule, S_g, to the singlet excited state of the dye, S_1^*. The rate of this reaction is a function of the wavelength-dependent photon flux, $h^\circ(\lambda)$, molar extinction coefficient of the dye molecule, $\hat{\varepsilon}(\lambda)$, and quantum yield of the dye molecule, $\Phi(\lambda)$. The solar radiation in terms of $h^\circ(\lambda)$ was obtained from the National Renewable Energy Laboratories database, the extinction coefficient of N719 dye was measured experimentally, and the quantum yield was obtained from Gratzel.[1] The rate of this reaction decays along the nanowire length according to Beer's Law and it is a function of the available dye in the ground state, S_g. It is important to note that this absorbance model neglects the absorbance of the nanowire core and shell material as well as the electrolyte that permeates the photoanode. In addition, the expression for r_2 does not include photonic or plasmonic interactions that could occur in ordered structures.[28] Reactions 3a and 3b (Table 1) represent the relaxation of the excited state of the dye molecule through an intermediate triplet state, S_3^*.

Reactions 4a and 4b (Table 1) represent the injection of an electron from either S_1^* or S_3^* into the conduction band of the semiconductor. However, photogenerated electrons can also be lost to the electrolyte through reactions 6a and 6b. (Table 1) The rates associated with reactions 4a and 4b, 6a and 6b (Table 1) are dependent only on the concentration of the respective excited

Table 1. Interfacial Reactions and Their Corresponding Rates

reaction no.	reaction	rate
(1a)	$A\,\text{Red} + n\gamma \underset{k_{b,1a}}{\overset{k_{f,1a}}{\rightleftharpoons}} B\,\text{Ox} + ne^-$	$\dfrac{i_{1a}}{i^o_{1a,\,ref}} = \left(\dfrac{C_{\text{Red}}}{C_{\text{Red},\infty}}\right)^A \left(\dfrac{C_\gamma}{C_{\gamma,\infty}}\right)^n \exp[b_a(\phi_{sh} - \phi_{el} - \phi^o_{1a})] - \left(\dfrac{C_{\text{Ox}}}{C_{\text{Ox},\infty}}\right)^B \left(\dfrac{C_e}{C_{e,\infty}}\right)^n \exp[-b_c(\phi_{sh} - \phi_{el} - \phi^o_{1a})]$
(2)	$S_g + h\nu \rightarrow S_1^*$	$r_2 = \displaystyle\int \Phi(\lambda)\hat{\varepsilon}(\lambda)C_{S_g}l_o \ln(10)h^o(\lambda)\exp[-\hat{\varepsilon}(\lambda)C_{S_g}\ln(10)l_o\tilde{Z}]\mathrm{d}\lambda$
(3a)	$S_1^* \xrightarrow{k_{3a}} S_3^*$	$r_{3a} = k_{3a}l_o C_{S_1^*}$
(3b)	$S_3^* \xrightarrow{k_{3b}} S_g$	$r_{3b} = k_{3b}l_o C_{S_3^*}$
(4a)	$S_1^* + \gamma \xrightarrow{k_{4a}} S^+ + e^-$	$r_{4a} = k^o_{4a}l_o C_{S_1^*}\exp[b_a(\phi_{sh} - \phi^o_{S_1^*})]$
(4b)	$S_3^* + \gamma \xrightarrow{k_{4b}} S^+ + e^-$	$r_{4b} = k^o_{4b}l_o C_{S_3^*}\exp[b_a(\phi_{sh} - \phi^o_{S_3^*})]$
(5)	$S^+ + e^- \xrightarrow{k_{5b}} \gamma + S_g$	$r_5 = -k^o_5 l_o C_e\dfrac{C_{S^+}}{C_{S_T}}\exp[-b_c(\phi_{sh} - \phi^o_{S^+})]$
(6a)	$B\,\text{Ox} + nS_1^* \xrightarrow{k_{b,6a}} nS^+ + A\,\text{Red}$	$r_{6a} = -k^o_{b,6a}l_o C^n_{S_1^*}\exp[-b_c(\phi^o_{S_1^*} - \phi_{el})]$
(6b)	$B\,\text{Ox} + nS_3^* \xrightarrow{k_{b,6b}} nS^+ + A\,\text{Red}$	$r_{6b} = -k^o_{b,6b}l_o C^n_{S_3^*}\exp[-b_c(\phi^o_{S_3^*} - \phi_{el})]$
(7)	$A\,\text{Red} + nS^+ \xrightarrow{k_{f,7}} B\,\text{Ox} + nS_g$	$r_7 = k^o_{f,7}l_o C^n_{S^+}\left(\dfrac{C_{\text{Red}}}{C_{\text{Red},\infty}}\right)^A \exp[b_a(\phi^o_{S^+} - \phi_{el})]$

state of the dye (S_1^* or S_3^*) since the ultra fast electron kinetics cause these reactions to be limited by the concentration of the corresponding species. Rates for reactions 4a and 4b (Table 1) were assumed to be only anodic in direction with the potential driving force given by the difference between the interfacial potential of the semiconductor and either the S_1^* or S_3^* electronic state, i.e., $(\phi_{sh} - \phi^o_{S_1^*})$ and $(\phi_{sh} - \phi^o_{S_3^*})$, respectively. Similarly, rates for reactions 6a and 6b are considered to be purely cathodic and represent two loss mechanisms to the photogenerated current that are dependent on the change in interfacial potential, i.e., $(\phi^o_{S_1^*} - \phi_{el})$ and $(\phi^o_{S_3^*} - \phi_{el})$, respectively.

Reaction 5 (Table 1) is the only other loss mechanism considered in this study. Upon injection of the electron from the excited state of the dye into the conduction band of the semiconductor, the electron can be lost to the oxidized state of the dye, S^+. This reaction rate is dependent on both the interfacial concentration of electrons as well as the concentration of S^+. The rate of reaction 5 (Table 1) is taken to be purely cathodic in direction, and the reaction is driven by the difference in interfacial potential, i.e., $(\phi_{sh} - \phi^o_{S^+})$.

Reaction 7 (Table 1) describes the regeneration of the oxidized state of the dye, S^+, by electron donation from the reduced-state ion, Red, in the electrolyte. The rate of reaction 7 (Table 1) is dependent on both the concentration of Red and S^+ and is considered to be purely anodic. Once again, the driving force of this reaction is the difference between the potential of each state, i.e., $(\phi^o_{S^+} - \phi_{el})$.

Under steady-state conditions, balances on the individual electronic states of the dye yield

$$0 = -r_2 + r_{3b} - r_5 + nr_7 \tag{6}$$

$$0 = r_2 - r_{3a} - r_{4a} + nr_{6a} \tag{7}$$

and

$$0 = r_{3a} - r_{3b} - r_{4b} + nr_{6b} \tag{8}$$

for S_g, S_1^*, and S_3^*, respectively. Addition of eqs 6 to 8 yields a more convenient result that equates the flux of charge on either side of the interface, i.e.,

$$0 = r_{4a} + r_{4b} + r_5 - n(r_{6a} + r_{6b} + r_7) \tag{9}$$

Thus, the concentrations of each dye state can be calculated from eqs 7–9 once the interfacial values for ϕ_{sh}, ϕ_{el}, C_e, C_{Ox}, and C_{Red} are known.

■ BULK CHARGE CARRIER TRANSPORT IN THE SEMICONDUCTOR AND ELECTROLYTE REGIONS

Equilibrium in the system can be defined by equating the electrochemical potential of charge carriers in the semiconductor to the ions in the electrolyte. The electrochemical potential, μ_i, for each charged species, i, is defined as

$$\mu_i = \mu^{\text{ref}}_i + RT\ln(C_i\hat{\gamma}_i) + z_iF\phi_j \tag{10}$$

where j denotes the region (i.e., semiconductor or electrolyte) in which the potential ϕ_j is being evaluated. The activity coefficient, $\hat{\gamma}_i$, in eq 10 is assumed to be unity in this study.

The flux of species i is proportional to the product of the concentration and the gradient of the electrochemical potential, i.e.,

$$\vec{N}_i = -u_iC_i\vec{\nabla}\mu_i \tag{11}$$

where the charge carrier/ionic mobility, u_i, can be related to the diffusion coefficient by the Einstein–Smoluchowski relation written in macroscopic units as $u_i = D_i/RT$.

Because of the high degree of confinement associated with the semiconductive shell, this region is not electrically neutral. In other words, the shell thickness is much less than the depletion region thickness defined by the Debye length of the

semiconductor. Thus, the potential is given by Poisson's equation,

$$\nabla^2 \phi_j = -\frac{F}{\varepsilon_j} \rho_j \tag{12}$$

where ρ_j is the charge density given by

$$\rho_j = \sum_i z_{i,j} C_{i,j} \tag{13}$$

Finally, the gradient of the flux within the semiconductor is distributed according to the net rate of homogeneous production and/or consumption of each charged species,

$$\vec{\nabla} \cdot \vec{N}_i = R_{\text{net},i} \tag{14}$$

The $\vec{\nabla}$ operators in eqs 11, 12, and 14 are scaled to a one-dimensional derivative according to eqs 1 and 2. Thus, the equations governing charge transport and the potential distribution within the semiconductor are given as

$$\frac{\partial^2 \phi_{\text{sh}}}{\partial \tilde{R}^2} = -\tau_{\text{sh}}^2 \frac{F}{\varepsilon_{\text{sh}}} (\hat{N}_a - C_e) \tag{15}$$

$$N_{e,\tilde{R}} = \frac{D_e}{\tau_{\text{sh}}} \left(-\frac{\partial C_e}{\partial \tilde{R}} + f C_e \frac{\partial \phi_{\text{sh}}}{\partial \tilde{R}} \right) \tag{16}$$

and

$$\frac{\partial N_{e,\tilde{R}}}{\partial \tilde{R}} = \tau_{\text{sh}} R_{\text{net,e}} \tag{17}$$

where $N_{e,\tilde{R}}$ is the flux solely in the radial direction and $f = F/RT$. Once again, hole transport was not considered, and the concentration of vacant conduction band states was taken to be $C_\gamma = \Gamma - C_e$ so that $R_{\text{net,e}}$ can be described by a simple band-to-band kinetic model.[29]

Equations 10–14 are utilized again for the electrolyte outside the diffuse double layer with the exception that the region was assumed to be electrically neutral. Thus, the potential distribution is given by

$$\vec{\nabla} \phi_j = -\frac{\acute{\iota}}{\kappa} - \frac{F}{\kappa} \sum_i z_i D_i \vec{\nabla} C_i \tag{18}$$

where the current is given by

$$\acute{\iota} = \sum_i z_i \vec{N}_i$$

and the conductivity is given by

$$\kappa = F^2 \sum_i z_i^2 u_i C_i$$

The equations that govern concentration and potential distribution within the diffusion layer of the electrolyte are

$$\frac{\partial \phi_{\text{el}}}{\partial \tilde{R}} = -\tau_{\text{el}} \frac{\acute{\iota}}{\kappa} - \frac{F}{\kappa} \sum_i z_i D_i \frac{\partial C_i}{\partial \tilde{R}} \tag{19}$$

$$N_{\text{Ox},\tilde{R}} = \frac{D_{\text{Ox}}}{\tau_{\text{el}}} \left(-\frac{\partial C_{\text{Ox}}}{\partial \tilde{R}} + f C_{\text{Ox}} \frac{\partial \phi_{\text{el}}}{\partial \tilde{R}} \right) \tag{20}$$

$$N_{\text{Red},\tilde{R}} = \frac{D_{\text{Red}}}{\tau_{\text{el}}} \left(-\frac{\partial C_{\text{Red}}}{\partial \tilde{R}} + f C_{\text{Red}} \frac{\partial \phi_{\text{el}}}{\partial \tilde{R}} \right) \tag{21}$$

$$\frac{\partial N_{\text{Ox},\tilde{R}}}{\partial \tilde{R}} = 0 \tag{22}$$

$$\frac{\partial N_{\text{Red},\tilde{R}}}{\partial \tilde{R}} = 0 \tag{23}$$

and

$$\frac{\partial C_C}{\partial \tilde{R}} + f C_C \frac{\partial \phi_{\text{el}}}{\partial \tilde{R}} = 0 \tag{24}$$

where C_C is the concentration of the counterion.

Transport of ions in the axial direction ($\tilde{Z}$-direction) was neglected in these scaled equations. A subsequent study will include contributions to the flow of ions in the $\tilde{Z}$-direction, which becomes more important when considering photoanodes with longer nanowires.

■ BOUNDARY CONDITIONS

Twelve boundary conditions were needed to solve the above differential equations. For the semiconductor region, the potential at the semiconductor—metal contact is the applied potential, and the concentration of electrons was assumed to be proportional to the ratio of the electron flux and the electric field, i.e.,

$$C_e(\tilde{R}_{\text{sh}} = 0) = \frac{\tau_{\text{sh}} RT N_{e,\tilde{R}}}{FD_e \dfrac{\partial \phi_{\text{sh}}}{\partial \tilde{R}}} \tag{25}$$

which can be obtained from the electron diffusion—migration equation, eq 16, under the assumption that the diffusion contribution to electron flux is negligible. The metal—semiconductor interface was assumed to be an ideal ohmic contact with no accumulation of charge. The flux of electrons through the semiconductor region was defined by the net rate of production from the interfacial kinetic model. As seen in Figure 3, the net reaction rate entering the conduction band is given by reactions 1a, 4a, 4b, and 5 (Table 1) such that

$$N_{e,\tilde{R}} = -[(1-\theta)nr_{1a} + \theta(r_{4a} + r_{4b} + r_5)] \tag{26}$$

Likewise, the fluxes of the charge carriers at the interface in the electrolyte are

$$N_{\text{Ox},\tilde{R}} = (1-\theta)Br_{1a} + \theta(r_{6a} + r_{6b} + r_7) \tag{27}$$

$$N_{\text{Red},\tilde{R}} = -[(1-\theta)Ar_{1a} + \theta(r_{6a} + r_{6b} + r_7)] \tag{28}$$

Furthermore, the current at any point in the axial direction, $\tilde{Z}$, is given by

$$\acute{\iota}\left(\tilde{Z}, V\right) = -nN_{e,\tilde{R}} = nN_{\text{Ox},\tilde{R}} = -nN_{\text{Red},\tilde{R}}$$

Gauss' Law holds that the potential gradient must be continuous across boundaries that do not represent planes of charge. Thus, at the OSS,

$$\left.\frac{\partial \phi_{\text{sh}}}{\partial \tilde{R}}\right|_{\tilde{R}_{\text{sh}} \to 1} = \tau_{\text{sh}} \frac{\phi_{\text{int}} - \phi_{\text{sh}}^{\text{OSS}}}{\delta_{\text{sh}}} \tag{29}$$

and, at the OHP,

$$\left.\frac{\partial \phi_{\text{el}}}{\partial \tilde{R}}\right|_{\tilde{R}_{\text{el}} \to 1} = \tau_{\text{el}} \frac{\phi_{\text{el}}^{\text{OHP}} - \phi_{\text{int}}}{\delta_{\text{el}}} \tag{30}$$

Table 2. Constants Used for the Numerical Model

constant	value	notes
$C_{e,\infty}/\hat{N}_a$	1.66×10^{-8} mol/cm^3	bulk electron concentration/dopant level[10,30]
$C_{Ox,\infty}$	5×10^{-5} mol/cm^3	Ox concentration (provided by Solaronix)
$C_{Red,\infty}$	4.5×10^{-4} mol/cm^3	Red concentration (Provided by Solaronix)
C_{S_T}	$7.5\ S_V^{-1} \times 10^{-5}$ mol/cm^2	total dye concentration
D_e	5 cm^2/s	electron diffusion coefficient in single-crystal anatase TiO$_2$
D_{Ox}, D_{Red}	5×10^{-5} cm^2/s	Ox and Red diffusion coefficient
$i_{1a,ref}^o$	5×10^{-13} mA/cm^2	reaction 1a (Table 1) exchange current density[5]
k_{3a}^o	6.67×10^{12} s^{-1}	standard rate constant for r_{3a}[31]
k_{3b}^o	1.67×10^6 s^{-1}	standard rate constant for r_{3b}[32]
k_{4a}^o	1.0×10^{13} s^{-1}	standard rate constant for r_{4a}[5,31]
k_{4b}^o	5.0×10^{10} s^{-1}	standard rate constant for r_{4b}[31]
k_5^o	5.0×10^4 s^{-1}	standard rate constant for r_5[5]
k_{6a}^o	1.0×10^2 s^{-1}	standard rate constant for r_{6a}[33]
k_{6b}^o	1.0×10^2 s^{-1}	standard rate constant for r_{6b}[33]
k_7^o	1.0×10^8 s^{-1}	standard rate constant for r_7[33]
Γ	1.125×10^{-3} mol/cm^3	density of states for anatase TiO$_2$[34]
δ_{sh}	0.2 nm	double layer thickness of semiconductor shell
δ_{el}	1 nm	double layer thickness of electrolyte
$\tilde{N}_{nw}$	10^{10} cm^{-2}	nanowire density
φ	0.5	porosity of photoanode
$\phi_{S_1^*}$	-1.3 V vs SCE	singlet excited state energy level of dye[33]
$\phi_{S_3^*}$	-0.75 V vs SCE	estimated triplet excited state energy level of dye based on ref 35
ϕ_{S^+}	0.5 V vs SCE	oxidized energy level of dye[33]

where τ_j in each equation arises from scaling $\tilde{R}_j$, δ_j is the double layer thickness, and the potentials are referenced to the OSS and OHP for the semiconductor and electrolyte, respectively. The ISS, associated with electrons in surface states, and the IHP, associated with adsorbed ionic species, were assumed to be located at the same position and were assigned the potential ϕ_{int}. The ISS, OSS, interfacial, IHP, and OHP planes are shown in Figure 3. The charge held in the interfacial plane is related to potential though Gauss' Law, i.e.,

$$\frac{\varepsilon_{sh}}{\delta_{sh}}\left(\phi_{sh}^{OSS} - \phi_{int}\right) - \frac{\varepsilon_{el}}{\delta_{el}}\left(\phi_{int} - \phi_{el}^{OHP}\right) = \frac{F}{S_V}C_{S^+} \quad (31)$$

The boundary conditions in the electrolyte are that the potential at the symmetric boundary between nanowires is zero. In addition, all electrolyte concentrations have their bulk values at the outer boundary of the diffusion layer.

■ COMPUTATIONAL DETAILS

The parameters used in the model are listed in Table 2. It is important to note that the standard rate constants listed in Table 2 are assumed not to deviate from those measured in NP-DSSC systems for Ru-based dyes. Therefore, the standard rate constants are independent of the energy levels in the dye–semiconductor–electrolyte interface, while the rates in Table 1 are dependent on these differences. The model and boundary conditions were discretized using a central difference approximation and solved using an algorithm that varied the root-finding scheme between a Newton's method and the method of steepest descent. This allowed the search-direction step size to vary, depending on how far the system was from the converged solution. The system of equations was broken into three sets: those describing the interfacial model, eqs 7–9, and the bulk charge transport in the semiconductor, eqs 15–17, and electrolyte, eqs 19–24. Additionally, the state variables in each system were scaled to

the order of 1 through an eigenvalue matrix. The interfacial boundary conditions coupled each set of the charge transport equations. As each system converged to an acceptable tolerance (10^{-20}), a fixed point iteration was performed between the two systems of equations. The fixed point iteration continued until both the interfacial boundary conditions were satisfied and the shared interfacial variables converged to equivalent values about each fixed point to a tolerance of 10^{-10}. Furthermore, initial guesses were chosen on the basis of either known fixed constants, such as bulk concentrations, or assumptions about the anticipated device performance. Multiple initial guesses were used to avoid local minima.

The current at each voltage was obtained by using a variable point Gaussian quadrature method to integrate the local current at any point $\tilde{Z}$, $\hat{i}(\tilde{Z},V)$, over the length of the nanowire

$$\hat{i}(V) = S_V\varphi\int_0^1 \hat{i}(\tilde{Z}, V)d\tilde{Z} \quad (32)$$

where φ is the photoanode porosity. Furthermore, the photoactive surface area to cell volume ratio, S_V, is related to the nanowire number density, $\tilde{N}_{nw}$ by

$$S_V = 2\pi(r_o + 2\tau_{sh})\tilde{N}_{nw} + \frac{1}{l_0} \simeq 2\pi(r_o + 2\tau_{sh})\tilde{N}_{nw} \quad (33)$$

where the two terms in eq 33 account for the surface area of the nanowire and the projected surface area. Once a solution is found at a designated applied potential, this solution is used as the initial guess for subsequent potentials. Convergence was better when the initial potential calculated was slightly negative.

As described in the SI, the potential distributions and concentration profiles for the relevant species were checked in each region to ensure the solution met the required boundary conditions. Figure S1(SI) shows that NW-DSSCs have potential differences across the semiconductor region that can generate large electric fields. Furthermore, Table S6 (SI)

18669

dx.doi.org/10.1021/ja2044216 | J. Am. Chem. Soc. 2011, 133, 18663–18672

shows the effect of various constants on short-circuit current. The solution is sensitive to the values of k_{3a}, k_{3b}, k_{4a}, k_{4b}, k_5, and D_{Red}. As shown in Figure 3, these rate constants are responsible for the concentration of dye in the excited state and the injection of the electron into the conduction band. While the solution was most sensitive to the primary injection rate constant (k_{4a}), this rate constant has been well studied,[5,31] and the value should not deviate significantly from that listed in Table 2.

■ EXPERIMENTAL DETAILS

Anodic aluminum oxide (AAO) templates were fabricated directly on ITO.[36] The pores were widened to remove the barrier layer, facilitating the adhesion of the nanowires during electrodeposition. In-doped ZnO (IZO) nanowires were then deposited inside the porous template.[37] The IZO nanowires were electrodeposited using an aqueous solution of 0.1 M hydrated $Zn(NO_3)_2$ and 0.75−1.0 mM $InCl_3$ that was pH-adjusted to 2.56 with HCl. After electrodeposition, the AAO template was selectively etched, using our previously reported drying method aided by electrostatic repulsion.[38] The nanowire array was then placed into a custom, atomic layer deposition chamber (Planar Systems, Inc.) for growth of the shell around each nanowire. The titania shells were deposited by cycling $TiCl_4$ and H_2O pulses separated by dry nitrogen purges, where 1 cycle represents the sequence consisting of 1 s H_2O/1 s purge/1 s $TiCl_4$/1 s purge. The N719 organic dye (Solaronix) was chemisorbed onto the core−shell nanowire array by heating the nanowire array to 200 °C and immersing it in 0.3 mM N719/ethanol for 12 h. The substrates were subsequently rinsed with dry ethanol and stored in an argon glovebox until used. The cell was completed by immersing it in an iodide REDOX couple (Iodolyte, Solaronix) and connecting it to a thermally platinized counter electrode. Hot melt spacers with a thickness of 40 μm (Surlyn 1702, DuPont) were used to sandwich and seal the counterelectrode to the photoanode. The electrolyte was introduced via capillary action. The devices were tested immediately after electrolyte immersion under AM 1.5 simulated sunlight (Solar Light, Inc.) using a potentiostat (Princeton Applied Research, Versastat 3).

■ RESULTS AND DISCUSSION

The numerical results obtained by the model were compared to experimental polarization curves. In addition, the role of the interfacial electric field, which is only present in NW-based DSSCs, was explored by comparison of numerical results obtained with and without the migration term in the flux expressions for electrons.

Calculated Device Performance and Experimental Comparison. A comparison between the calculated and experimental polarization curves for DSSCs based on both IZO and ZnO nanowires[22] is presented in Figure 4. Both of these nanowire systems have a titania shell thickness of 10 nm, which was found to be the optimal thickness in the experimental devices. The performance of the DSSCs based on ZnO arrays is better, but this photoanode has much larger surface area since the nanowires are 6 times longer. The dye uptake was quite good for the IZO nanowire arrays, and it was assumed that the surface coverage, θ, was equal to 0.85. On the other hand, a smaller value of 0.77 was assumed for the ZnO-based DSSC since Law et al. attributed its poor performance to low dye coverage.

The model was able to capture some of the qualitative and quantitative features of the experimental polarization curves. In both devices, the short-circuit current, i_{sc}, was well represented by the model. The small disparity in i_{sc} could be due to errors in experimental measurement of the device area. Note that the
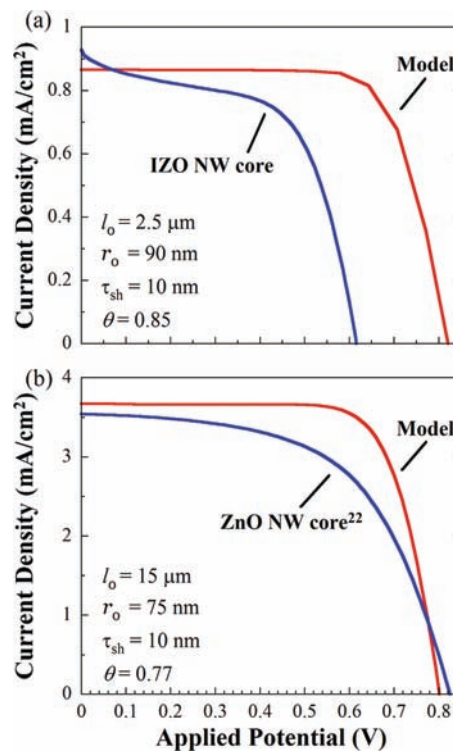
**Figure 4.** Comparison of experimental and calculated polarization curves for NW-DSSCs based on titania-coated (a) 2.5 μm long IZO and (b) 15 μm long ZnO nanowires.[22]

physics needed to describe the lowered shunt resistance (estimated by the inverse slope at i_{sc}) found in the IZO-based DSSCs of Figure 4a is not included in the model. While the model was able to predict the open-circuit voltage, V_{oc}, for the NW-DSSCs based on ZnO (within 2%), a significant deviation was observed for the NW-DSSCs based on IZO. The large deviation in V_{oc} for these devices is likely due to the poorly crystalline titania shell, which was also observed in some ZnO NW-DSSCs.[22] The major difference in the polarization curves of Figure 4 is the fill factor, which is a measure of device performance. In both nanowire devices, the model predicts high fill factors of 0.74 for both IZO and ZnO NW-DSSCs. However, the experimental data has lower fill factors of 0.62 and 0.58 for IZO and ZnO NW-DSSCs, respectively. These deviations in fill factor are likely associated with the fact that the model is assuming a conductive rather than semiconductive nanowire core. Thus, the electrons injected into the semiconductor region are quickly being swept away in the model results, allowing better charge transport and device performance. Interestingly, the series resistance of the curves for the NW-DSSCs based on IZO are nearly identical. The similarity is likely due to the fact that IZO is more conductive than ZnO.

Influence of Interfacial Electric Field. A key difference between NP- and NW-DSSCs is the presence of an interfacial electric field, which many researchers believe enhances the charge transfer and transport physics in the latter system. The different geometries of the systems and the inability to remove the effect of the electric field in experiments has made it difficult to quantify its importance in device performance. However, elimination of the electron migration term in eq 16 effectively turns the electric field OFF in the model. Therefore, comparison

18670

dx.doi.org/10.1021/ja2044216 |*J. Am. Chem. Soc.* 2011, 133, 18663–18672
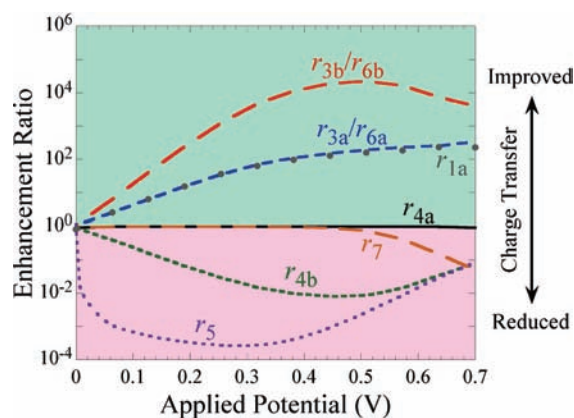
Figure 5. Comparison of the interfacial reaction rates for the ON and OFF states of the electric field. The enhancement ratio relates the ON and OFF states (written in the forward direction) to characterize the effect of the interfacial electric field on the performance of NW-DSSCs. Therefore, values greater than 1 indicate improved charge transport.

Figure 6. Comparison of the polarization curves for NW-DSSCs for the ON and OFF states of the electric field.

of the ON and OFF states of the electric field allows the benefits from a field to be quantified, especially the changes to species concentrations and the rates of charge transfer/transport processes. To depict succinctly the effect of the interfacial field on charge transfer reactions, each reaction was written in terms of an enhancement ratio. This ratio is defined in the direction of current flow so the ratio for back reactions (ratio of OFF/ON states) is opposite of the forward reactions (ON/OFF). An enhancement ratio of unity indicates that the field has no effect on the process, while values greater than unity indicate improvements to charge transfer due to the interfacial electric field.

The enhancement ratio for each reaction due to the electric field is shown in Figure 5. The most critical process within all DSSCs is the injection of the electron from the singlet state to the conduction band, which is given by r_{4a}. As can be seen from Figure 5, the primary injection rate from the singlet state remains essentially unchanged. The lack of changes is due to the fact that the dye is designed to heavily favor injection over back reaction. On the other hand, the back-reaction rate from the singlet state (r_{6a}) decreases by a factor of about 100 in the presence of an electric field. This indicates that the back reaction of primary electrons is 100 times slower in the presence of an interfacial electric field, providing significant benefits to charge transport. The decrease in electron injection from the triplet state (r_{4b}) is surprising. However, charge transport from the triplet state is less important than the primary dye state since the majority of the charge is concentrated in the singlet state. Further, this decrease is only 100 times smaller while the corresponding back reaction rate (r_{6b}) shows a 10,000-fold improvement to charge transfer. This difference effectively results in a 100-fold improvement to the charge transport of photogenerated electrons from the triplet state of the dye to the semiconductor. The excited states of the dye are also subject to relaxation mechanisms (r_{3a} and r_{3b}). The changes for these reactions follow the back reaction rates (r_{6a} and r_{6b}) very closely. The similarity is associated with the fact that the concentration of S_1^* and S_3^* dictate these rates. The improvement of these loss mechanisms is likely due to the improved charge transport that keeps the concentration of S_1^* and S_3^* lower. For this reason, the back-reaction rate for the direct loss of an electron from the conduction band to the electrolyte (r_{1a}) displays similar behavior. It should be noted that identical
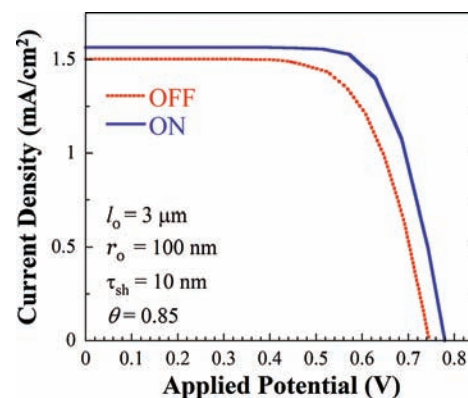
enhancement ratios do not mean that the reaction rates are the same but instead indicate that the effect of the electric field on the reaction is similar. For example, r_{1a}, r_{3a}, and r_{6a} have identical enhancement ratios but the rates are approximately 10^{-11}, 10^{-35}, and 10^{-15} s^{-1}, respectively.

Another electron-loss mechanism is the direct transfer of electrons from the semiconductor conduction band to the oxidized state of the dye (r_5). As shown in Table 1, this rate is a function of the concentration of conduction band electrons at the interface of the semiconductor and electrolyte. Because of the improved transport of electrons, it was expected that the rate would decrease. However, this electron loss rate increases when an interfacial electric field is present within the semiconductor, as shown in Figure 5. The change to the rate is quite substantial at low applied potentials but the loss mechanism reaches a minimum at an applied potential of 0.25 V and then becomes less affected. The change in behavior is due to the competing changes to electron and S^+ concentration between the ON and OFF states. At low potentials, the difference in electron concentration between the two states is high, but the effect starts to plateau at ~0.3 V. At ~0.4 V, the concentration of S^+ starts to drop in the ON state, which results in better rates for this back reaction.

Finally, the regeneration of the dye is described by reaction rate r_7. This reaction rate remains unaffected by the electric field until applied potentials are greater than 0.4 V. At these higher potentials, the electric field causes the reaction to be slower. This behavior is due to a reduction in S^+ concentration when the field is ON.

The various reaction pathways described above can be summarized by looking at the changes to device performance. The simulated current−voltage characteristics of a NW-DSSC with the field ON or OFF is shown in Figure 6. The shape of the curves are similar; however, the device with the field ON has small but significant increases to short-circuit current and open-circuit voltage. The field also improves the fill factor of the device (0.72 vs 0.68). Combining these changes to the current−voltage characteristics leads to approximately a 15% increase in efficiency, i.e., $\eta_{ON} \approx 1.15\eta_{OFF}$. It should be noted that the field OFF state cannot be directly related to NP-DSSCs since the model does not account for diffusion through the entire titania film. While the presence of an electric field in NW-DSSCs yields an appreciable gain in performance, these devices have substantially lower photoactive surface area than NP-DSSCs

(often more than 75% lower). Therefore, the beneftis from the electric field will not likely improve performance of NW- over NP-DSSCs without comparable photoactive surface area.

CONCLUSIONS

This report introduces a continuum-based mathematical model of DSSCs based on nanowire arrays as the photoanode. The model results were in quantitative and qualitative agreement with experimental polarization curves. The ability to neglect artificially the effect of electron migration in the model, i.e., ignore the interfacial electric field present in nanowire systems, allowed its importance to specific interfacial charge-transfer reactions to be evaluated. The calculations showed that the electric field dramatically decreases photoexcited electron back reactions without a significant decrease to electron injection. The enhanced transport from the electric field leads to better short-circuit current, open-circuit voltage, and fill factor of the device. While these results show moderate improvements to performance, the components of NW-DSSCs can be further optimized to take full advantage of the benefits from the electric field.

ASSOCIATED CONTENT

S **Supporting Information.** Variable lists, concentration profiles, potential distributions, and sensitivity analysis. This material is available free of charge via the Internet at http://pubs.acs.org.

AUTHOR INFORMATION

Corresponding Author
kziegler@che.ufl.edu

Present Address
[‡]Mainstream Engineering, Rockledge, Florida 32955, United States

ACKNOWLEDGMENT

REFERENCES

(1) Gratzel, M. *J. Photochem. Photobiol., A* **2004**, *164*, 3–14.
(2) Gao, F.; Wang, Y.; Shi, D.; Zhang, J.; Wang, M.; Jing, X.; Humphry-Baker, R.; Wang, P.; Zakeeruddin, S.; Gratzel, M. *J. Am. Chem. Soc.* **2008**, *130* (32), 10720–10728.
(3) Gratzel, M.; Frank, A. J. *J. Phys. Chem.* **1982**, *86*, 2964–2967.
(4) Gratzel, M. *Nature* **2001**, *414*, 338–344.
(5) Hagfeldt, A.; Gratzel, M. *Chem. Rev.* **1995**, *95*, 49–68.
(6) Toyoda, T.; Sano, T.; Nakajima, J.; Doi, S.; Fukumotoa, S.; Ito, A.; Tohyamaa, T.; Yoshida, M.; Kanagawa, T.; Motohiro, T.; Shiga, T.; Higuchi, K.; Tanaka, H. *J. Photochem. Photobiol., A* **2004**, *164*, 203–207.
(7) O'Regan, B.; Gratzel, M. *Nature* **1991**, *353*, 737–740.
(8) Schlichthorl, G.; Huang, S. Y.; Sprague, J.; Frank, A. J. *J. Phys. Chem. B* **1997**, *101* (41), 8141–8155.
(9) Albery, W. J.; Bartlett, P. N. *J. Electrochem. Soc.* **1984**, *131*, 315–325.
(10) Ferber, J.; Luther, J. *J. Phys. Chem. B* **2001**, *105*, 4895–4903.
(11) Peter, L. *J. Electroanal. Chem.* **2007**, *599*, 233–240.
(12) Ferber, J.; Stangl, R.; Luther, J. *Sol. Energy Mater. Sol. Cells* **1998**, *53*, 29–54.
(13) Nelson, J.; Chandler, R. E. *Coord. Chem. Rev.* **2004**, *248*, 1181–1194.
(14) Penny, M.; Farrell, T.; Please, C. *Sol. Energy Mater. Sol. Cells* **2008**, *92*, 11–23.
(15) Penny, M.; Farrell, T.; Will, G. *Sol. Energy Mater. Sol. Cells* **2008**, *92*, 24–37.
(16) Villanueva-Cab, J.; Wang, H.; Oskam, G.; Peter, L. M. *J. Phys. Chem. Lett.* **2010**, *1* (4), 748–751.
(17) Peter, L. M.; Wijayantha, K. G. U. *Electrochim. Acta* **2000**, *45*, 4543–4551.
(18) Duffy, N. W.; Peter, L. M.; Wijayantha, K. G. U. *Electrochem. Commun.* **2000**, *2*, 262–266.
(19) Pasquier, A. D.; Chen, H.; Lu, Y. *Appl. Phys. Lett.* **2006**, *89*, 253513–253516.
(20) Adachi, M.; Murata, Y.; Takao, J.; Jiu, J.; Sakamoto, M.; Wang, F. *J. Am. Chem. Soc.* **2004**, *126* (45), 14943–14949.
(21) Law, M.; Greene, L. E.; Johnson, J. C.; Saykally, R.; Yang, P. D. *Nat. Mater.* **2005**, *4*, 455–459.
(22) Law, M.; Greene, L. E.; Radenovic, A.; Kuykendall, T.; Liphardt, J.; Yang, P. *J. Phys. Chem. B* **2006**, *110*, 22652–22663.
(23) Wang, H.; Ting, C.; Hung, M.; Chiou, C.; Liu, Y.; Liu, Z.; Ratinac, K.; Ringer, S. *Nanotechnology* **2009**, *20*, 055601.
(24) Gubbala, S.; Chakrapani, V.; Kumar, V.; Sunkara, M. K. *Adv. Funct. Mater.* **2008**, *18*, 2411–2418.
(25) Bisquert, J.; Zaban, A.; Greenshtein, M.; Mora-Sero, I. *J. Am. Chem. Soc.* **2004**, *126* (41), 13550–13559.
(26) Zaban, A.; Greenshtein, M.; Bisquert, J. *Chem. Phys. Chem. Comm.* **2003**, *4*, 859–865.
(27) Orazem, M. E.; Newman, J. *J. Electrochem. Soc.* **1984**, *131* (11), 2569–2574.
(28) Kelzenberg, M. D.; Boettcher, S. W.; Petykiewicz, J. A.; Turner-Evans, D. B.; Putnam, M. C.; Warren, E. L.; Spurgeon, J. M.; Briggs, R. M.; Lewis, N. S.; Atwater, H. A. *Nat. Mater.* **2009**, *9*, 239–244.
(29) Asano, T.; Kubo, T.; Nishikitani, Y. *Jpn. J. Appl. Phys.* **2005**, *44*, 6776–6780.
(30) Zaban, A.; Meier, A.; Gregg, B. A. *J. Phys. Chem. B* **1997**, *101*, 7985–7988.
(31) Asbury, J. A.; Anderson, N. A.; Hao, E.; Ai, X.; Lian, T. *J. Phys. Chem. B* **2003**, *107*, 7376–7379.
(32) Smestad, G.; Bignozzi, C.; Argazzi, R. *Sol. Energy Mater. Sol. Cells* **1994**, *32*, 259–265.
(33) Hagfeldt, A.; Gratzel, M. *Acc. Chem. Res.* **2000**, *33*, 269–272.
(34) Kambili, A.; Walker, A. B.; Qiu, F. L.; Fisher, A. C.; Savin, A. D.; Peter, L. M. *Physica E* **2002**, *14*, 203–205.
(35) Junghanel, M. Novel aqueous electrolyte films for hole conduction in dye sensitized solar cells and development of an electron transport model. Ph.D. Thesis, 2007.
(36) Hill, J. J.; Haller, K.; Ziegler, K. J. *J. Electrochem. Soc.* **2011**, *158*, E1–E7.
(37) Hill, J. J. Photoelectrochemical Energy Conversion in Nanowire-Based Dye-Sensitized Solar Cells: Modeling, Optimization and Templated Fabrication. Ph.D. Thesis, University of Florida, Department of Chemical Engineering, 2010.
(38) Hill, J. J.; Haller, K.; Gelfand, B.; Ziegler, K. J. *ACS Appl. Mater. Int.* **2010**, *7*, 1992–1998.